

Submitted to The Astrophysical Journal

THREE-DIMENSIONAL MHD SIMULATIONS OF RADIATIVELY INEFFICIENT ACCRETION FLOWS

Igor V. Igumenshchev

*Laboratory for Laser Energetics, University of Rochester, 250 East River Road, Rochester,
NY 14623; iigu@lle.rochester.edu*

Ramesh Narayan

*Department of Astronomy, Harvard-Smithsonian Center for Astrophysics, 60 Garden
Street, Cambridge, MA 02138; narayan@cfa.harvard.edu*

Marek A. Abramowicz

*Department of Astronomy and Astrophysics, Göteborg University and Chalmers University
of Technology, S-41296, Göteborg, Sweden; marek@fy.chalmers.se*

ABSTRACT

We present three-dimensional MHD simulations of rotating radiatively inefficient accretion flows onto black holes. In the simulations, we continuously inject magnetized matter into the computational domain near the outer boundary, and we run the calculations long enough for the resulting accretion flow to reach a quasi-steady state. We have studied two limiting cases for the geometry of the injected magnetic field: pure toroidal field and pure poloidal field. In the case of toroidal field injection, the accreting matter forms a nearly axisymmetric, geometrically-thick, turbulent accretion disk. The disk resembles in many respects the convection-dominated accretion flows found in previous numerical and analytical investigations of viscous hydrodynamic flows. Models with poloidal field injection evolve through two distinct phases. In an initial transient phase, the flow forms a relatively flattened, quasi-Keplerian disk with a hot corona and a bipolar outflow. However, when the flow later achieves steady state, it changes in character completely. The magnetized accreting gas becomes two-phase, with most of the volume being dominated by a strong dipolar magnetic field from which a thermal low-density wind flows out. Accretion occurs mainly via narrow slowly-rotating radial streams which ‘diffuse’ through the magnetic field with the help of magnetic reconnection events.

Subject headings: accretion, accretion disks — black hole physics — convection
— MHD — turbulence

1. INTRODUCTION

This study is a continuation of our efforts during the last several years to understand the nature of underluminous accreting black holes. A class of radiatively inefficient solutions (Ichimaru 1977; Rees et al. 1982; Narayan & Yi 1994, 1995a,b; Abramowicz et al. 1995; Narayan, Mahadevan & Quataert 1998) has been influential in this field. A key feature of these solutions is that radiative energy losses are small so that most of the energy is advected with the gas. Narayan & Yi (1994) came up with the name ‘advection-dominated accretion’ to describe such flows, and Lasota (1996) suggested the acronym ADAF (advection-dominated accretion flow). Usually by ADAFs one understands optically thin accretion flows with very low mass accretion rates, $\dot{M} \ll \dot{M}_{Edd}$, but ADAFs are also possible as optically thick flows with high accretion rates, $\dot{M} > \dot{M}_{Edd}$, where \dot{M}_{Edd} is the Eddington accretion rate. In the later case, one uses the name ‘thick accretion disks’ (see e.g. Jaroszyński, Abramowicz & Paczyński, 1980) or ‘slim accretion disks’ (Abramowicz et al., 1988) rather than ADAFs.

Historically, ADAFs were initially studied within the framework of viscous hydrodynamics. In this approach, one assumes that the accreting gas has an ‘anomalous viscosity’ parameterized by the standard dimensionless viscosity parameter α . Early analytic work revealed that the gas in an ADAF would be (i) gravitationally unbound because of a positive Bernoulli parameter, which might lead to a strong outflow (Narayan & Yi 1994, 1995a), and (ii) convectively unstable (Gilham 1981; Begelman & Meier 1982; Narayan & Yi 1994, 1995a). The important role of these processes was not, however, realized until numerical two- and three-dimensional hydrodynamic simulations were carried out by a number of authors (Igumenshchev, Chen & Abramowicz 1996; Igumenshchev & Abramowicz 1999, 2000; Stone, Pringle & Begelman 1999; Igumenshchev, Abramowicz & Narayan 2000; McKinney & Gammie 2002). These studies showed that the behavior of a viscous ADAF depends on the value of α . If α is large, say > 0.3 , then there is a powerful bipolar outflow driven by the positive Bernoulli parameter. However, if α is small, say < 0.1 , the flow is dominated by convective motions which strongly modify the structure of the flow.

The convection-dominated low- α case was modeled analytically by Narayan, Igumenshchev & Abramowicz (2000) and Quataert & Gruzinov (2000), who coined the name ‘convection-dominated accretion flow’ (CDAF). Two key features of a CDAF are: (i) the Reynolds stress associated with the convective turbulence moves angular momentum inward

rather than outward, and (ii) the density profile is much flatter than in the case of a pure ADAF — $\rho \sim R^{-1/2}$ rather than $R^{-3/2}$. The CDAF model provides a physical explanation for the low luminosity accreting black holes: the luminosity is reduced because of the mass accretion rate is much reduced in the presence of convection.

Accretion models that are based on the principles of viscous hydrodynamics are limited by the fact that they need to invoke a mysterious ‘anomalous viscosity.’ It is generally believed that the ‘viscosity’ in these models is provided by magnetic fields via the magneto-rotational instability (Balbus & Hawley 1991). If this is the case, then a deeper understanding of accretion flows can clearly be obtained by analyzing the problem directly within the framework of MHD. Numerical MHD simulations of radiatively inefficient flows have been carried out recently by a number of authors (Hawley 2000, 2001; Stone & Pringle 2001; Machida, Matsumoto & Mineshige 2001; Hawley, Balbus & Stone 2001; Hawley & Balbus 2002; Casse & Keppens 2002). However, the results obtained by these authors have not been entirely consistent. For instance, some authors conclude that radiatively inefficient MHD flows behave like CDAFs (Machida et al. 2001), whereas others claim that the flows are very different (Hawley et al. 2001). It is not clear if the discrepancies arise from differences in the assumed geometry of the initial magnetic field or differences in the numerical techniques.

We present in this paper 3D numerical simulations that we have carried out of radiatively inefficient MHD accretion flows. In §2 we describe our numerical method and the initial and boundary conditions. In §3 we present numerical results for two topologies of the injected magnetic field: toroidal field (§3.1) and poloidal field (§3.2). In §4 we discuss the implications of our results. We argue that the toroidal field case has many points of similarity with the CDAF model (§4.1), while the poloidal field case behaves very differently (§4.2). In fact, the steady state configuration that we obtain for the poloidal problem is unlike anything published previously in the literature; we suggest possible reasons for this (§4.3). In §5 we conclude with a summary.

2. SIMULATION TECHNIQUE

2.1. Magnetohydrodynamic Equations and Numerical Method

We consider the dynamics of accreting plasma within the framework of the one-fluid MHD approximation. The relevant equations of resistive MHD take the following form:

$$\frac{d\rho}{dt} + \rho \nabla \cdot \mathbf{v} = 0, \tag{1}$$

$$\rho \frac{d\mathbf{v}}{dt} = -\nabla(P_g + Q) - \rho \nabla \Phi + \frac{1}{4\pi} (\nabla \times \mathbf{B}) \times \mathbf{B}, \quad (2)$$

$$\rho \frac{d\epsilon}{dt} = -(P_g + Q) \nabla \cdot \mathbf{v} + \frac{1}{4\pi} \eta \mathbf{J}^2, \quad (3)$$

$$\frac{\partial \mathbf{B}}{\partial t} = \nabla \times (\mathbf{v} \times \mathbf{B} - \eta \mathbf{J}), \quad (4)$$

where ρ is the density, \mathbf{v} is the velocity, P_g is the gas pressure, Φ is the gravitational potential, \mathbf{B} is the magnetic induction, ϵ is the specific internal energy, $\mathbf{J} = \nabla \times \mathbf{B}$ is the current density, η is the resistivity, and Q is the additional ‘pressure’ corresponding to a standard artificial viscosity.

We adopt the ideal gas equation of state,

$$P_g = (\gamma - 1) \rho \epsilon, \quad (5)$$

with an adiabatic index $\gamma = 5/3$, and we assume that there is no radiative cooling. We neglect self-gravity of the gas and take the gravitational potential to be entirely due to a central black hole of mass M . We employ a pseudo-Newtonian approximation (Paczynski & Wiita 1980) for the potential:

$$\Phi = -\frac{GM}{R - R_g}, \quad R_g = \frac{2GM}{c^2}, \quad (6)$$

where R measures the radial distance from the black hole and R_g is the gravitational radius of the black hole.

Our numerical method is the MHD generalization of the hydrodynamic PPM algorithm (Colella & Woodward 1984) and is identical to that used by Igumenshchev & Narayan (2002). In this method the hydrodynamical part is solved by means of a variant of the Godunov method and the magnetic part is solved using a modified version of the method of characteristics (Stone & Norman 1992). To avoid excessive loss of energy as a result of numerical reconnection of magnetic field lines, the resistivity is assumed to be non-zero and to have the following form,

$$\eta = \eta_0 \frac{|\nabla \times \mathbf{B}|}{\sqrt{4\pi\rho}} \Delta^2, \quad (7)$$

where η_0 is a dimensionless parameter and Δ is the grid spacing.

The code operates on a three-dimensional nested Cartesian grid, which is designed so as to adequately resolve the large range of spatial scales spanned by the accretion flow. We designate the distance from the black hole to the face centers of the outermost cube of the grid as R_{out} . Please see Igumenshchev & Narayan (2002) for a more detailed discussion of the code.

2.2. Initial and Boundary Conditions

The simulations are begun with non-magnetized ‘empty space’ surrounding the black hole; for technical reasons the empty space corresponds in actuality to a non-zero but extremely low density of matter. Mass is steadily injected into the computational domain inside a slender equatorial torus of thickness equal to about two grid-cells centered on the black hole and with a radius nearly equal to R_{out} . The injected matter has Keplerian rotation velocity and internal energy equal to a fraction 0.2 of the gravitational energy. The matter also has a magnetic field associated with it. We have adopted two configurations for the injected field: purely toroidal field and purely poloidal field (defined with respect to the equatorial plane of the torus).

In the toroidal injection case, the field is generated assuming that only the vertical component A_z of the vector potential \mathbf{A} is non-zero in the injected matter; the other two components, A_r , A_ϕ , are set to zero. Here and below, we represent \mathbf{A} in cylindrical coordinates (r, ϕ, z) . In each time step, A_z is increased within the torus as follows,

$$A_z^{\text{new}} = A_z^{\text{old}} + \left(\frac{8\pi\Delta\rho c_s^2}{\beta_0} \right)^{1/2} \Delta, \quad (8)$$

where $\Delta\rho$ is the increase of the density in the torus due to the injection of matter and c_s^2 is the sound speed of the injected matter. The parameter β_0 measures the plasma β of the injected material ($\beta \equiv P_g/P_m$ where P_m is the magnetic pressure). Since the injection of matter is axisymmetric, this model generates magnetic field with closed axisymmetric toroidal magnetic lines. In reality, however, the finite resolution of the Cartesian grid introduces small non-axisymmetric perturbations to the field structure. These act as seed perturbations in the simulations.

Magnetic field with poloidal topology is generated in a similar way as described above, with the same functional form given in equation (8), except that now only the component A_ϕ is taken to be non-zero, and A_r and A_z are both set to zero. In this case, the injected magnetic field lines take the form of poloidal loops around the torus.

In both the toroidal and poloidal cases, the presence of magnetic field in the injected material allows the redistribution of angular momentum via magnetic stresses. As a result, some of the injected matter loses its initial angular momentum and accretes onto the black hole, while the excess angular momentum is removed from the computational domain by the rest of the matter flowing out. With time, the initial inner ‘empty space’ becomes filled with accreting gas, and after several rotation periods as measured at the injection radius, a quasi-stationary accretion flow is established. We are mainly interested in the inner regions of the accretion flow, where the influence of the outer boundary and the injection region is

not significant. Test simulations show that the dynamics and structure of the flow inside $\sim R_{out}/2$ depends only weakly on the details of the injection region.

Absorbing boundary conditions are applied at both the inner and outer boundaries. The inner boundary consists of an *absorbing sphere* of radius $R_{in} = 2 R_g$ located inside the marginally stable orbit of the black hole, while the outer boundary corresponds to the outermost cube of the Cartesian grid at R_{max} . At both the inner and outer boundaries, matter is allowed to flow freely out of the computational domain, but no matter is allowed to return from outside. Magnetic field at both boundaries satisfies the divergence-free condition. The field at the inner boundary is defined assuming that $\mathbf{A} = \mathbf{A}_{init} = \text{constant}$ in the ghost cells located inside R_{in} ; here \mathbf{A}_{init} is the initial (uniform) vector potential. This boundary condition on \mathbf{A} introduces a jump in the magnetic field near R_{in} . However, the jump has no effect on the inflowing matter because of the strong gravity and super-Alfvénic infall speed. At the outer boundary, the transverse components of the field with respect to the sides of the cube are assumed to be zero. This again introduces a jump in the field, which results in an artificial torque on the flow. The strength of this spurious torque increases with increasing field strength.

3. NUMERICAL RESULTS

The simulations were done on a Cartesian numerical grid consisting of a number of nested subgrids of increasing resolution inward. The grid is designed to provide extra resolution closer to the black hole. The number of subgrids varies from 1 to 5 in different runs. Each subgrid consists of $64 \times 64 \times 64$ cells. The cell size in the innermost subgrid is $\Delta_1 = 0.5R_g$, and each succeeding subgrid has its cell size increased by a factor of 2. Therefore, in the simulations with 5 subgrids, the outermost subgrid has $\Delta_5 = 8R_g$, and covers a cube of size $2R_{out} \times 2R_{out} \times 2R_{out}$, where $R_{out} = 256R_g$. In practice, we use only a quarter of the full cubic domain, by focusing on a 90° wedge around the z -axis. Thus, we employ $32 \times 32 \times 64$ cells along xyz and use periodic boundary conditions in the azimuthal direction. The nested Cartesian grid has an important technical advantage with respect to a conventional spherical grid: there are no polar singularities, and therefore there is no reduction in the azimuthal grid-size near the pole. As a result, the time step defined by the Courant condition is significantly longer compared to a spherical grid, and for a given amount of computational effort we are able to run a simulation for a much longer time.

All our models have been calculated assuming the resistivity parameter $\eta_0 = 0.3$. It has been found in previous MHD simulations (Igumenshchev & Narayan 2002) that this value of η_0 is reasonable. On the one hand, η_0 is small enough that it does not excessively smooth

out small-scale magnetic structures. At the same time it is large enough to prevent serious loss of energy through numerical field reconnection.

3.1. Simulations with Toroidal Injected Field

The first set of simulations we describe involve the injection of matter with a toroidal field topology. These simulations were done with $A_r = A_\phi = 0$ and with A_z is equal to the value given in equation (8). As explained in §2.2, this leads to a purely toroidal injected field. As the accreting matter moves in, however, poloidal field of either sign is generated locally, though the total magnetic flux through the equatorial plane is still zero to within the accuracy of truncation errors.

We have calculated a range of models with different values of the parameter β_0 (which describes the strength of the injected magnetic field) and with different numbers of nested Cartesian subgrids. We find that the flow pattern in steady-state is practically independent of β_0 . The magnetic field in the inner regions of the flow reaches a saturation level which is almost the same for β_0 anywhere in the range 1 to 10^4 . The reason is that the magnetic field adjusts near the injection region itself to a certain saturation level, and maintains that level at all smaller radii. Machida et al. (2001) also found that the flow structure is independent of the initial strength of the toroidal magnetic field.

We discuss here our most advanced simulation, Model A, which was calculated on 5 subgrids with an outer radius $R_{out} = 256R_g$ and injected field parameter $\beta_0 = 10^2$. By the end of the simulation, Model A achieved steady state in a time-averaged sense. Figure 1 shows a snapshot of the density distribution in this model in meridional cross-section. We see that the accreting matter forms a thick disk, in which the density is concentrated at the equatorial plane and increases toward the black hole. The small-scale fluctuations of density which are visible are due to turbulent motions. The amplitude of the fluctuations is not large. Figure 2 shows a snapshot of the pressure distribution, which is seen to have even smaller amplitude fluctuations compared to the density. This is because the turbulence is subsonic.

The turbulent motions in the gas in Model A are generated by magnetic interactions, which provide the main dissipation mechanism. Most of the dissipation of energy arises from the resistive term, $\eta\mathbf{J}^2/4\pi$, in equation (3); the contribution from the artificial viscosity is very low since there are no shocks. During accretion, the binding energy of matter is efficiently converted into magnetic energy by two distinct mechanisms: field dragging by the radially converging flow (Shvartsman 1971), and field amplification by a magnetic dynamo

associated with the magneto-convection and turbulence. In Fig. 3, we show a schematical example of how the local magnetic field may be amplified. A perturbed magnetic line is stretched in the azimuthal direction by the Keplerian differential rotation, following which the line self-reconnects, leaving behind a closed magnetic loop in addition to the original line. This mechanism represents a non-linear stage of the magneto-rotational instability (Balbus & Hawley 1991). Field amplification is accompanied by field dissipation via magnetic reconnection, which releases energy locally at the reconnection site. The combined effect of a large number of reconnection events, randomly distributed in time and over the disk volume, drives the turbulent motions and fluctuations in the flow.

One finds thus a feedback link between turbulence and reconnection: the turbulent motion tangles magnetic lines and amplifies the magnetic field, the tangled lines and turbulent motion increase the number of reconnection events, and the reconnections feed the turbulent motions through local dissipation of the field. Obviously, there is a saturation state in which the rate of amplification of magnetic energy is balanced by the rate of dissipation via reconnection.

In Fig. 4 we show a typical example of the topology of the magnetic lines as projected on the equatorial plane. We see that the lines are not simply stretched tangentially as we would expect for a pure Keplerian flow. Rather, the lines are strongly perturbed by the presence of many magnetic loops. In the meridional section shown in Fig. 5, we again see that reconnection and turbulent motion of matter result in a very complicated topology of poloidal magnetic lines. Especially in the equatorial regions, we see many magnetic vortices and loops of different spatial scales. In contrast, in the narrow polar regions, the magnetic topology is dominated by a regular field, in which magnetic lines are oppositely directed in the upper and lower funnels.

Figure 6 shows a snapshot of the plasma β in meridional cross-section. We see that β is highly inhomogeneous as a result of the stochastic reconnection and local dissipation of magnetic field described above. In individual fluctuations, the magnetic pressure can be up to $\sim 1 - 2$ orders of magnitude larger than the average value. However, the gas pressure P_g fluctuates very little and P_m never exceeds P_g . On average, $\beta \sim 10^2 - 10^3$ in the equatorial region of the accretion flow, and decreases towards the poles.

The dissipation of magnetic field via reconnection results in an increase in the entropy of the local gas. Figure 7 shows the distribution of the specific entropy in meridional cross-section. We see that the entropy increases with decreasing radius in the equatorial plane, and increases from the equator to the poles at a given radius. The entropy distribution shows significant inhomogeneities in the form of tangled filaments. These can be explained in terms of convective motions in the unstably stratified medium. Indeed, the convective motions

seen in this MHD model suggest that the flow is closely related to the CDAF discovered in viscous hydrodynamical simulations (§1). In particular, Figure 8 show that in Model A the time-averaged surfaces of constant specific entropy are closely aligned with those of specific angular momentum. This effect, noticed already for convective thick accretion disks by Bardeen (1970) and Paczyński & Abramowicz (1982), and found in viscous hydrodynamic simulations by Igumenshchev et al. (1996) and Stone et al. (1999), indicates that the medium is marginally stable with respect to the Høiland criterion (Tassoul 1978). The polar regions of the flow, however, are filled with matter that has a very low density and high entropy and there is no convection there. We discuss the connection between Model A and the CDAF model in more detail in §4.1.

Figure 9 shows a snapshot of the flow streamlines in Model A projected on a meridional cross-section. Most of the flow is dominated by time-dependent vortices of different spatial scales. Matter accretes by gradually moving toward the black hole, passing through these vortices. Only in the narrow polar directions do the streamlines show regular inflow into the black hole. However, the accretion rate there is relatively small because of the low density. Figure 10 shows the time-averaged flow pattern, averaged over about three Keplerian rotation periods measured at R_{out} . The pattern consists of stationary large scale ($\sim R$) meridional circulation cells. Thus, even the time-averaged flow shows deviations from a simple radial pattern.

We should emphasize that neither the snapshot in Fig. 9 nor the time-averaged flow pattern in Fig. 10 exhibits any tendency to produce a significant bipolar outflow of mass. In Fig. 10, there is an equatorial outflow inside a radius $R \simeq 10R_g$. Other than this, there is no evidence for an outflow or a jet, in agreement with a general theoretical argument by Abramowicz, Lasota & Igumenshchev (2000).

Figure 11 shows time-averaged radial profiles of selected gas properties on the equatorial plane. The upper left panel shows the density ρ . Leaving aside the spiky outer region near the injection radius and the innermost region near the black hole, we see that the density follows a roughly power-law behavior with radius, say over the range $R \simeq 10 - 100R_g$. The upper right panel shows the specific angular momentum ℓ . We see that the rotation is super-Keplerian over a small range of radius near the outer boundary, is sub-Keplerian over much of the intermediate region, and is nearly Keplerian near the black hole. The overall behaviour is similar to that found in global models of thick disks, slim disks and ADAFs (e.g., Jaroszyński et al. 1980; Abramowicz et al. 1988; Narayan, Kato & Honma 1997; Chen, Abramowicz & Lasota 1997). The super-Keplerian nature of ℓ near the injection point was discussed by Abramowicz, Igumenshchev, & Lasota (1998). The lower left panel shows the radial velocity v_R , which is found to have a very non-regular behaviour. This is explained

by the meridional circulation patterns seen in the time-averaged flow shown in Fig. 10. The spikes in the plot are due to changes in the sign of the velocity. The lower right panel shows the ratio c_s/v_K , which characterizes the relative thickness of the flow: $H/R \simeq c_s/v_K$. The ratio does not change much with radius.

Over the interior of the flow, between about $10R_g$ and $100R_g$, we find approximately that $\rho \propto R^{-1}$, $c_s \propto R^{-0.5}$, and $\ell \propto \ell_K \sim R^{1/2}$. The radial velocity v_R does not show a very clear power-law behavior.

Figure 12 shows the average total stress $T_{R\phi}$ in meridional cross-section:

$$T_{R\phi} = \overline{\rho\delta v_R\delta v_\phi} - \overline{\rho\delta v_{AR}\delta v_{A\phi}} \equiv T_{R\phi}^R + T_{R\phi}^{mag}, \quad (9)$$

where $T_{R\phi}^R$ is the Reynolds stress associated with fluid motions and $T_{R\phi}^{mag}$ is the Maxwell stress associated with magnetic field fluctuations. In the definition of the latter, $\delta\mathbf{v}_A \equiv \delta\mathbf{B}/\sqrt{4\pi\rho}$ represents the fluctuations in the Alfvén speed due to field fluctuations. We find that $T_{R\phi}$ is nearly axisymmetric. Figure 12 shows that the sign of $T_{R\phi}$ behaves non-monotonically over much of the flow. Regions of negative $T_{R\phi}$ form regular structures which are extended in the vertical direction and are strongly correlated with the locations of circulation patterns in Fig. 10. In particular, there is an extended region of negative $T_{R\phi}$ at intermediate angles between the poles and the equator, where angular momentum is transported inward. Near the equator, however, the angular momentum is on average transported outward. We discuss the behavior of the stress in greater detail in §4.1.

Simulations on nested Cartesian grids can suffer from artificial perturbations in the flow at subgrid interfaces. These perturbations are due to the sudden change in the resolution across subgrids, which can introduce errors in interpolation. To check the influence of these errors in our simulations, we have calculated several test models on a spherical grid. These simulations showed good qualitative and quantitative agreement with models calculated on the nested Cartesian grid, indicating that any perturbations due to the presence of subgrids are weak. Although the spherical grid has important advantages on account of its simple and monotonic structure, we found that it is not practical to use it for the full range of simulations. This is because models on a spherical grid require significantly smaller time steps on account of the Courant condition near the poles (see the discussion at the beginning of §3).

3.2. Simulations with Poloidal Injected Field

The previous section described simulations with a toroidal injected field. Here we describe analogous models with a poloidal field. In these simulations, we assumed that the injected gas has a vector potential with $A_r = A_z = 0$ and a non-zero A_ϕ . The range of

β_0 that we have used varies from 10^2 to 10^4 , which means that the injected field is always much below equipartition strength. We find that decreasing β_0 speeds up evolution of the model to the steady-state; however, as in the toroidal case, the final steady-state does not depend on β_0 . We have simulated several low resolution models on the nested Cartesian grid, using 1 – 2 subgrids. We refer to our representative model, calculated on 2 subgrids with $R_{out} = 64 R_g$, as Model B. Because of the low resolution of the models, in the following we focus only on qualitative aspects of the evolution of the models.

The Keplerian differential rotation of the injected material stretches the poloidal magnetic lines in the azimuthal direction. This leads to a redistribution of angular momentum and spreading of the matter in the radial direction. A good fraction of the injected gas moves outward and leaves the computational domain. The rest moves inward and forms an accretion flow. At the beginning of the simulations, the magnetic field in the injection torus has zero net B_z . At later times, however, as the outflowing matter leaves the computational domain and carries away magnetic field of predominantly one sign of B_z , the inflowing matter drags magnetic field with the opposite sign of B_z inward. As a result, the accretion flow acquires a non-zero net B_z .

We find that the evolution of the accretion flow goes through two distinct stages. First, there is a transient stage during which the gas in the injection torus spreads out and forms an accretion disk stretching down to the black hole. This transient stage is then followed by a quasi-steady state in which the magnetic field exerts a significant back-pressure on the accreting gas.

In the transient stage, the geometry of the flow is very similar to that described by Hawley, Balbus & Stone (2001) in their 3D simulations of non-radiative MHD flows. The accreting gas forms a nearly Keplerian disk with a vertically extended low-density corona. The magnetic field has a simple dipolar topology near the outer boundary, but tends to be complicated at smaller radii, with toroidal fields of opposite directions above and below the disk. The field experiences reconnection events which cause the matter in the equatorial region to be locally heated up. Due to the combined effects of reconnection heat, toroidal magnetic field pressure and the centrifugal mechanism (Blandford & Payne 1982), a fraction of the disk matter is ejected in the vertical directions to feed the low density corona. The corona is mostly in dynamical equilibrium, but a small fraction of the matter in it forms a hot, low density, high velocity, bipolar outflow. The outflow carries a significant fraction of the liberated energy in the form of kinetic energy, heat and Poynting flux. As a result, the accretion disk, though quite hot, is not as hot or thick as in Model A.

With increasing time, the above transient phase is replaced by a steady state configuration with very different properties. The change occurs because the dipole magnetic field

that is dragged inward by the accretion flow, accumulates in the vicinity of the black hole. Note that, while gas can fall into the black hole and disappear, open field lines cannot vanish. With time, the accumulated dipole field becomes quite strong and its influence begins to extend to large radii. When the magnetic energy density reaches equipartition with the thermal energy density of the disk, the magnetic pressure is strong enough to suppress accretion. After this time, matter can move toward the black hole only by ‘diffusing’ through the field, which it does by means of local interchanges followed by reconnection. The simulations show that the accreting matter becomes significantly sub-Keplerian and is no longer disk-like. Instead, the matter forms narrow and very slowly rotating streams, which radially penetrate the highly magnetized low density medium near the black hole.

With time, the region over which the accumulated field dominates increases in size until it finally fills the entire computational domain. At this point, the model has reached a quasi-steady-state in which the net magnetic flux no longer changes significantly with time. Instead, any new magnetic field line which is injected with new matter is pushed out through the outer boundary by the magnetic pressure. Matter, however, can decouple from the field, ‘diffuse’ through the existing magnetic lines along the radial narrow streams mentioned above and fall into the black hole.

Figure 13 shows the distribution of density in Model B in this steady-state. Four streams are seen as an increase of density in the equatorial plane. The accretion velocity in the streams is significantly sub-sonic and sub-Alfvénic. The topology of the magnetic lines in meridional cross-section is shown in Fig. 14. We see that the magnetic field is dominated by a strong dipolar component. The magnetic $\beta \sim 10^{-3} - 10^{-4}$ in the regions away from the streams, and ~ 1 within the streams. Surfaces of constant total pressure ($P_g + P_m$) are nearly spherical. Figure 15 shows the structure of the magnetic field projected on the equatorial plane. The structure is complicated and time-dependent, reflecting the irregular character of field dissipation in the dense accreting streams and low density coronal medium.

4. DISCUSSION

The results described in §3 show that the nature of a radiatively inefficient MHD accretion flow is very different depending on whether the injected material is dominated by toroidal or poloidal fields. In §§4.1 and 4.2 below we compare the results we have obtained for these two limiting cases to our previous work on viscous hydrodynamic and MHD flows. Then, in §4.3, we compare our results to simulations done by other groups.

4.1. Toroidal Field Injection

Model A, which involves the injection of matter with a toroidal field configuration, has a number of distinct features (§3.1). Field amplification and reconnection leads to a significant level of heating in many localized regions spread all over the flow. The heating causes the average entropy to increase as a function of decreasing radius, as well as to increase from the equator to the pole (Fig. 7). Since the gradient of the entropy tends to be unstable (by the Høiland criterion), convective motions are set up which lead to considerable turbulence in the medium. We see evidence for this turbulence in all the diagnostics we have considered: density (Fig. 1), pressure (Fig. 2), magnetic field (Fig. 4, 5), plasma β (Fig. 6), velocity streamlines (Fig. 9, 10). The well-developed turbulent eddies ensure that fluid elements cannot accrete smoothly down to the black hole from large radius, but rather must random walk through a series of eddies. This has the effect of suppressing the mass accretion rate onto the black hole.

Convection in radiatively inefficient accretion flows, or ADAFs, has been discussed for several years, mostly in the context of viscous hydrodynamics. The possibility of convection in ADAFs was emphasized by Narayan & Yi (1994, 1995ab), but the surprisingly strong effect that convection has on the flow was not appreciated until numerical simulations were carried out by Igumenshchev & Abramowicz (1999) and Stone et al. (1999). Igumenshchev & Abramowicz (2000) found that convection is most important when the viscosity is weak, specifically when the viscosity parameter α is less than about 0.1. This and other studies also showed that convection has the effect of suppressing the mass accretion rate onto the black hole.

Using the hydrodynamic simulations as a guide, Narayan et al. (2000) and Quataert & Gruzinov (2000) developed an analytical model describing a new form of radiatively inefficient accretion called CDAF. The model has two important features.

First, it postulates that convection transports angular momentum inward rather than outward; that is, the Reynolds stress, $T_{R\phi}^R$, associated with the fluid fluctuations is negative. The viscous stress is, however, always outward, i.e., $T_{R\phi}^{visc} > 0$. Thus, there is a competition between convection and viscosity. In fact, the two fluxes almost cancel each other in a CDAF so that the net angular momentum flux is much smaller than either of the fluxes individually: $0 < T_{R\phi}^R + T_{R\phi}^{visc} \ll |T_{R\phi}^R|, |T_{R\phi}^{visc}|$.

Second, convection drives an outward energy flux F_c , which dominates over other forms of energy transport. As a result, the flow is driven to a state of constant convective luminosity with radius, i.e., $4\pi R^2 F_c = \text{constant}$. Narayan et al. (2000) and Quataert & Gruzinov (2000) showed that this immediately implies that the density should scale as $\rho \sim R^{-1/2}$.

Both effects cause the mass accretion rate to be reduced. Note that the first of the two effects is specific to rotating flows, whereas the second can occur in either rotating or non-rotating flows. Indeed, Igumenshchev & Narayan (2002) showed that spherical accretion of a non-rotating magnetized plasma leads to strong convection, which causes many of the effects seen in rotating CDAFs: constant convective luminosity, density varying as $R^{-1/2}$, and suppressed mass accretion.

The presence of well-developed convection in Model A suggests that this rotating MHD model may be similar to a CDAF. For instance, Model A has a relative disk thickness, $H/R \simeq 0.5$, a flattened density profile, and nearly Keplerian rotation, all of which make it similar to the CDAF model shown for instance in Fig. 17 of Igumenshchev & Abramowicz (2000). There is, however, a controversy in the literature on whether or not an MHD flow can behave like a CDAF. Balbus & Hawley (2002), based on linear analysis, claimed that it is highly unlikely that there could be modes in an MHD accretion flow that transport angular momentum inward (see also Christodoulou, Contopoulos & Kazanas 2002, who come to a similar conclusion), whereas Narayan et al. (2002) argued that convective modes in an MHD medium can transport angular momentum inward provided the mode wavelength λ is long enough; specifically, they required $\lambda/H \gg \beta^{-1/2}$.

Figure 12 shows the distribution of total stress $T_{R\phi}$ in the meridional plane of Model A. We see that the stress is both positive and negative in different regions, which makes it hard to identify in which direction angular momentum flows on average. Figure 16 shows separately the spherically averaged Reynolds stress $T_{R\phi}^R$ (filled dots) and Maxwell stress $T_{R\phi}^{mag}$ (open circles) as functions of the radius. Each quantity has been calculated over spherical shells of thickness equal to the inner radius. Thus, the average over a shell from R to $2R$ is plotted at the geometric mean radius $\sqrt{2}R$, the average from $2R$ to $4R$ is plotted at $2\sqrt{2}R$, etc. In comparing the results to the idealized CDAF model, it should be noted that the Maxwell stress in an MHD medium plays the same role as the viscous stress $T_{R\phi}^{visc}$ in a viscous hydrodynamic flow.

Despite the coarse averaging procedure we have used which corresponds to heavy smoothing, the results are unfortunately still noisy. This is a consequence of the fact that there are large-scale circulation patterns in the flow which introduce correspondingly large-scale effects on the stress (e.g., Fig. 12). Nevertheless, some effects appear to be clear. First, we see that the Maxwell stress is always positive, i.e., the magnetic stress always moves angular momentum outward, just as viscosity does in the hydrodynamic case. Secondly, and more importantly, we see that over a good fraction of the interior of the flow (i.e., away from the boundaries), the Reynolds stress tends to be negative, i.e., the convective eddies move angular momentum inward. The sum of the two stresses is always positive, which

means that angular momentum is moved outward on average. These features are qualitatively similar to what is seen in a hydrodynamic CDAF and suggest that MHD flows with toroidal field injection are analogous to the CDAF. One should keep in mind, however, that the numerical results are noisy. Note also that there is not a near cancellation of the two stresses, as expected in the idealized CDAF model. Rather, the Maxwell stress dominates over the Reynolds stress (as indeed expected by Balbus & Hawley 2002). This may be the result of the relatively coarse resolution and small radial dynamic range of the present simulations. Another possible consequence of the net outward angular momentum flux is that the MHD CDAF could consist of two distinct parts: almost non-rotating inner part and quasi-Keplerian rotating outer part (Igumenshchev 2002).

As mentioned above, another feature of the CDAF model is that the density has a shallow radial dependence, $\rho \sim R^{-1/2}$, compared to the steeper dependence, $\rho \sim R^{-3/2}$, expected in the absence of convective angular momentum transport (Narayan & Yi 1994). Fig. 11 shows that the density in Model A is indeed shallower than $R^{-3/2}$, which is consistent with the expectations of the CDAF model. However, the profile is not as shallow as $R^{-1/2}$, but rather appears to vary as $\sim R^{-1}$. One possible explanation for this discrepancy is that convection moves energy not only in the radial direction, as assumed in the simple one-dimensional CDAF model developed by Narayan et al. (2000) and Quataert & Gruzinov (2000), but also in the vertical direction. Imagine dividing the flow into an equatorial thick ‘disk’ region where most of the accretion occurs and a polar ‘corona’ region. In the disk region, apart from convective energy transport in the radial direction, there could also be vertical leakage of energy into the corona. Such a vertical component of the convective flux has been seen in viscous hydrodynamical simulations (e.g. Abramowicz, Björnsson & Igumenshchev 2000). Obviously, if there is a loss of energy from the disk, then the radial convective luminosity $R^2 F_c$ within the disk will not be independent of radius, as assumed in the CDAF model, but will decrease with increasing radius. It is easy to see that this will cause the density profile to steepen relative to the pure CDAF profile.

To be more quantitative, let us consider the same form of the energy equation as in Narayan et al. (2000), but with an additional cooling term Q^- to describe the vertical loss of energy,

$$\rho v T \frac{ds}{dR} + \frac{1}{R^2} \frac{d}{dR} (R^2 F_c) = Q^+ - Q^-, \quad (10)$$

where s is the specific entropy, T is the temperature, F_c is the outward convective energy flux through the disk and Q^+ is the energy dissipation rate per unit volume. In the CDAF solution, one neglects all the terms except the second one on the left and thereby finds that the convective luminosity $4\pi R^2 F_c$ is independent of radius. For the present case, let us retain

the cooling term and write

$$\frac{1}{R^2} \frac{d}{dR} (R^2 F_c) = -Q^-, \quad (11)$$

and let us specify Q^- by assuming that a fraction ξ of the outward flux F_c escapes in the vertical direction:

$$Q^- = \xi \frac{F_c}{H}. \quad (12)$$

In radiatively inefficient accretion flows the temperature is close to virial, so the outward convective flux can be estimated to be

$$F_c \propto \rho v_K^3 \propto \rho R^{-3/2}. \quad (13)$$

Substituting the estimate (13) into equation (11), we find that ρ varies as R^{-a} , where

$$a = \frac{1}{2} + \frac{\xi}{H/R}. \quad (14)$$

Equation (14) shows that, in the presence of an extra source of cooling as represented by a value of $\xi > 0$, the radial density profile becomes steeper than the canonical $R^{-1/2}$ of the CDAF model. Typically, we have $H/R \approx 0.5$. Thus, in order to explain the slope of $a \sim 1$ found in Model A, we require $\xi \sim 1/4$. Thus, about 25% of the local convective energy flux in the disk must escape into the corona.

It should be noted that, despite the modification described above, which allows for vertical loss of energy and a range of power-law indices a for the density, this model is still basically a CDAF, since it is convection that causes the index a to fall below $3/2$. Another model that has been discussed in the literature (Blandford & Begelman 1999) invokes heavy mass loss in an outflow as a result of a positive Bernoulli constant in the accreting gas (Narayan & Yi 1994, 1995ab). This model again leads to a range of values of a , but it is very different in spirit from the CDAF. In the mass outflow model, the mass accretion rate in the disk is large at large radii and decreases as one moves in. The excess mass is lost from the system in a powerful mass outflow. Model A does exhibit significant mass outflow only in the outermost region, near the radius where mass is initially injected into the simulation. Further in, there is practically no mass lost from the system. Rather, the gas here participates in convective eddies. Any fluid element that temporarily moves outward as a result of buoyancy turns around after going some distance and flows back toward the center. In this sense, Model A is closer in spirit to a CDAF than the mass outflow model of Blandford & Begelman (1999).

4.2. Poloidal Field Injection

Model B, in which the injected matter has a poloidal magnetic field, behaves completely differently from Model A. In an initial, transient stage, the gas in this model forms a relatively flattened disk, with a hot corona and a low-density, high-velocity, bipolar outflow. There is some qualitative analogy between this stage of the flow and what has been seen in viscous hydrodynamic simulations with large viscosity parameter $\alpha \sim 0.3 - 1$ (Igumenshchev & Abramowicz 2000). Those flows too have powerful unbound outflows. However, the analogy is not perfect. For example, the high- α hydro flows have a large accretion velocity and very sub-Keplerian rotation, whereas the MHD Model B described here has a small accretion velocity and nearly Keplerian rotation.

After the above transient phase, Model B settles down to a completely different configuration which is characterized by a strong dipolar field that fills the entire computational domain. The field builds up to this configuration during the transient phase as the accreting gas advects in magnetic field with the same sign of mean B_z . The accumulated field imposes strong constraints on the infalling gas. Once the steady state has been reached, any injected magnetic field is carried away from the computational domain by a fraction of the injected gas, while the rest of the gas, minus field, accretes onto the black hole via long slowly-rotating nearly-radial streams.

The reason for the buildup of magnetic field can be traced to the particular prescription we have used for the injected field, in which the vector potential \mathbf{A} is assumed to be independent of time. Because of this, we continuously inject matter with the same sense of poloidal field. The gas near the inner radius of the torus always has one sign of B_z and it is this gas that accretes onto the black hole, causing a steady buildup of the magnetic flux. The gas near the outer radius of the injection torus escapes from the computational domain, carrying away flux of the opposite sign.

This explains why we find such a profound difference between simulations with toroidal field injection (Model A) and poloidal field injection (Model B). In the former case, the injected gas has no net magnetic flux. Therefore, even though part of the gas accretes and part escapes, the part that accretes does not carry a net flux and there is no opportunity for the flux to build up near the black hole.

In a real accretion flow we imagine that the poloidal component of the injected field will fluctuate with time. If the fluctuations are slow so that the sign of B_z remains the same for much longer than the accretion time, then the flow ought to resemble what we see in Model B. There should be a transient period during which the gas would form a disk and would have an energetic outflow, followed by a long period of time during which the accretion

would be restricted to narrow streams. When the sign of the field finally reverses (assuming it does — see below), there will again be a transient disk-like phase with ejection in an outflow, and the cycle will repeat. During the transient stages, one would expect to observe powerful flare activity due to the annihilation of oppositely directed poloidal fields. On the other hand, if the poloidal field reverses its direction frequently, then we imagine that the accretion flow will resemble the initial transient phase of Model B at all times. Both cases could be investigated by repeating our simulations with a time-varying A_ϕ in the injected gas.

Somewhat analogous behavior to that described above has been seen in spherical MHD accretion. Igumenshchev & Narayan (2002) have simulated a case in which the external gas in Bondi accretion has a uniform magnetic field. They find that, as the gas flows in, the field around the black hole builds up, causing a back-reaction on the accreting gas. This is one of the reasons (though the main reason is convection) for causing the accretion rate to fall. The main difference between the Bondi simulation and Model B described here is the geometry of the injected mass. In the Bondi problem, the mass comes in spherically, whereas in Model B, the mass is injected in a torus with a disk-like geometry. With a disk-like source, there is a large solid angle of empty space through which a low density outflow can carry away energy and angular momentum. However, when the incoming mass has spherical symmetry, any gas that attempts to carry away energy is stopped by incoming gas. As a result, it is more efficient for the gas to transport energy via convective motions and this is what is seen in the Bondi simulation. As the magnetic field at the center builds up, however, the spherical symmetry is broken and the accreting matter in the inner regions takes the form of a doughnut (see Igumenshchev & Narayan 2002).

Both in the torus problem and in the spherical inflow problem, the long-term evolution of the magnetic field near the black hole depends on the statistics of the magnetic field in the externally supplied gas. One can easily imagine situations in which the accreted magnetic flux builds up to quite a high value and remains at that value for quite a long time. For instance, if the ΔB_z that is added with each new piece of matter is completely uncorrelated with previous injections, then the accreted magnetic flux would random-walk in time, and would on average increase as $t^{1/2}$. Alternatively, if the field in the injected matter is part of a turbulence spectrum with a large outer scale, then again one expects the flux to grow to a large value and to remain at that value for a long time. These arguments suggest that the steady state that we have observed in Model B may be relevant to many accreting black holes. Indeed, the very unusual effects we have seen, e.g., accretion via narrow slow-rotating streams, may not be restricted to radiatively inefficient accretion. A similar buildup of field and corresponding modification of gas dynamics could occur even in radiatively efficient accretion flows.

High-energy observations frequently suggest the simultaneous presence of hot nearly relativistic matter and ‘cold’ quasi-thermal gas in the inner regions of active galactic nuclei (AGN) and black hole X-ray binaries. Magnetic fields are believed to be a common ingredient in these systems, and it has been proposed that the field may effectively confine or otherwise couple to clumpy cold gas (Krolik 1998; Celotti & Rees 1999). Our Model B with poloidal field injection exhibits some of the features postulated in these proposals. Accretion occurs mostly as relatively cold gas, but the binding energy of this gas is released through magnetic reconnection and a large fraction of the heat goes into the hot phase. X/ γ -rays radiated by reconnecting magnetic flares in the hot phase, and reprocessed optical-UV radiation from the cold phase, may explain some of the spectral signatures observed in AGN and X-ray binaries.

4.3. Comparison with Previous MHD Simulations

Several groups have recently published results of 2D and 3D MHD simulations of radiatively inefficient accretion flows. Machida et al. (2001) studied the evolution of a rotating magnetized torus in which the magnetic field initially is purely toroidal. During the evolution, the torus forms a turbulent accretion flow with a flattened radial density profile. The authors state that their flow is similar to a CDAF, and indeed their simulation has many points of resemblance to our Model A. A detailed quantitative comparison of the two models is, however, difficult since their simulation extends over a limited range of radius, so that there are large boundary effects.

Stone & Pringle (2001), Hawley et al. (2001) and Hawley & Balbus (2002) have presented simulations of MHD nonradiative accretion flows starting from an initial torus of matter with a poloidal magnetic field. They find that the torus evolves with time and forms a rotationally supported disk-like accretion flow sandwiched between low-density coronal regions. The coronal regions form bipolar outflows. Magnetic field in the innermost regions of their model has a bipolar structure with non-zero net vertical flux. These features are similar to what we see in our Model B during its initial transient stage. However, there are two important details in the models of Hawley & Balbus (2002) which differ from our simulations. They report finding a small hot torus near the marginally stable orbit and a magnetically-confined jet near the rotation axis. These are not present in Model B. An even more important difference is that Hawley et al. (2001) and Hawley & Balbus (2002) do not see any accumulation of magnetic field in the vicinity of the black hole. Consequently, their simulations do not exhibit the kind of steady state configuration we have described in §3.2 in which the field dominates the dynamics and gas is able to accrete only via narrow radial

streams.

We believe that the above discrepancies between the simulations are the result of using different inner boundary conditions. We use an *absorbing sphere* inner boundary condition centered on the black hole (see §2.2). Thus, the black hole is the only absorbing entity, and the z -axis away from the black hole is a non-absorbing regular region of the flow. In contrast, Hawley and colleagues use an *absorbing cylinder* inner boundary condition, in which the region within $1.5R_g$ cylindrical radii of the z -axis is removed from the computational domain and absorbing boundary conditions are applied along this entire excised region. The two boundary conditions do not cause any significant differences for hydrodynamic simulations. However, the story is very different for MHD flows. Figure 17 schematically shows the difference between the two boundary conditions. When magnetized gas flows in, the net magnetic flux in the accretion flow is conserved if the absorbing sphere boundary condition is used. Thus, matter falls into the black hole, but open field lines do not disappear. In contrast, with the absorbing cylinder boundary condition, the component of the magnetic field parallel to the axis of the cylinder gets absorbed. Therefore, the simulation does not conserve the net magnetic flux. This is a serious problem, especially when, as in our Model B, the flow causes an accumulation of field near the black hole. In our simulation, the accumulated field remains in the computational volume and has a profound effect on the time evolution of the accretion flow. With the absorbing cylinder boundary condition, however, the field never has a chance to accumulate since it keeps disappearing at the axis. Therefore, one obtains an incorrect description (we believe) of MHD processes in the vicinity of the black hole.

The absorbing cylinder inner boundary condition is convenient and allows one to avoid certain technical problems near the rotation axis in 3D MHD simulations. Perhaps for this reason, a number of recent numerical simulations of MHD accretion flows around black holes have employed this boundary condition (e.g. Hawley 2000, 2001; Hawley & Krolik 2001, 2002; Armitage, Reynolds, & Chiang 2001; Krolik & Hawley 2002). The effect of the inconsistency pointed out above on these simulations needs to be investigated.

Recently, Casse & Keppens (2002) published results of 2D numerical simulations of a magnetized accretion disk with a polytropic equation of state. The authors assumed continuous injection of matter at the outer boundary and studied the case of an initially equipartition dipole magnetic field. They find that the large scale magnetic field extracts angular momentum from a nearly Keplerian disk, thereby inducing accretion and also creating bipolar outflows. Unfortunately, they evolved their model for only a very short time, less than an orbital period at the injection radius. Their results are consistent with those of Hawley and collaborators and also with our results on Model B during the early transient phase. However, since they have not run their model long enough, they are not in a position

to confirm the late-time field-dominated steady state that we find in Model B.

Most of the studies cited above have either not used explicit resistive terms in any of the MHD equations, or used resistivity only in the induction equation (4) but without accounting for resistive dissipation in the energy equation (the last term on the right in eq.[3]). These simplifications are likely to cause serious non-conservation of energy: one has a reduction of magnetic energy via numerical reconnection or resistive dissipation, but the reduction is not compensated for by a corresponding increase in the thermal energy (see §2.1). Note, in particular, that non-conservation of energy in magnetic reconnection will lead to a suppression of thermal convection (Igumenshchev & Narayan 2002). It is, therefore, not surprising that CDAF-type solutions are found only in simulations that treat energy conservation properly.

Simulations that reveal non-CDAF-type flows, like our Model B with poloidal injected field, or the models of Hawley and collaborators and Casse & Keppens (2002) above, are not very sensitive to energy conservation. The presence of a strong dipolar magnetic field causes most of the liberated energy in these flows to quickly escape over a wide solid angle in the polar regions, without any significant interaction with the equatorial accretion flow. The amount of energy that flows out may be different with different simulation techniques, depending on how well energy is conserved during field reconnection events, but this does not have much of an effect on the accretion flow.

5. SUMMARY

We have described in this paper global time-dependent three-dimensional MHD simulations of radiatively inefficient accretion flows onto black holes. The simulations are done within the framework of a pseudo-Newtonian potential to mimic relativistic effects near the black hole. The flows span a radial range from an inner radius $R_{in} = 2R_g$ to an outer radius R_{out} , which in different models ranges from $64R_g$ to $512R_g$. Magnetized matter is continuously injected into the computational domain within a torus whose major radius is slightly less than R_{out} and whose minor radius is about one grid cell. The material starts off with Keplerian rotation and no initial radial velocity. However, matter spreads under the influence of magnetic torques, and part of the injected matter accretes onto the black hole while the rest escapes from the computational box. The following is a summary of the main results.

1. We have studied two limiting cases for the geometry of the injected magnetic field: pure toroidal field and pure poloidal field. We find that the results are completely different

in the two cases.

2. When the injected field is primarily toroidal, which corresponds to the simulation designated Model A (see §3.1), the accreting gas forms a nearly axisymmetric, quasi-stationary, geometrically thick disk with little mass outflow in a wind or a jet.

3. The magnetic field achieves a saturation level with a plasma $\beta \sim 10^2$. In this saturated state, field amplification by radial convergence and dynamo action is balanced by field dissipation through reconnection.

4. There is considerable convective activity in the flow, driven by an unstable entropy gradient that results from energy dissipation via field reconnection.

5. There is a close analogy between our MHD Model A and the CDAF model that was developed to explain viscous hydrodynamic simulations of radiatively inefficient accretion flows. In particular, there is evidence that the Reynolds stress in the interior of the flow (away from the boundaries) moves angular momentum inward rather than outward.

6. The radial density profile is relatively flat, $\rho \sim R^{-1}$, but not as flat as the $\rho \sim R^{-1/2}$ predicted by the CDAF model. We suggest that the difference is because of the vertical leakage of convective energy flux from the thick disk (see §4.1).

7. Our results on the toroidal field case are similar to some previous work in the literature, but our simulations have a larger dynamic range and have been run for a longer time.

8. When the injected field is primarily poloidal, which corresponds to the simulation designated Model B (see §3.2), the accretion flow goes through two distinct phases.

9. In an initial transient phase, the accreting gas forms a relatively flattened axisymmetric disk with a hot corona and a bipolar outflow. This stage is similar to results found by other groups.

10. With time, as the accreting gas continues to bring in magnetic flux, the magnetic field builds up both around the black hole and farther out. The strong field disrupts the axisymmetry of the disk, leading to a completely different steady state flow configuration.

11. In steady state, there is a two-phase medium. Most of the volume is filled with a strong dipolar magnetic field with $\beta \ll 1$, from which a thermal wind flows out along the open magnetic lines. Accretion occurs mainly via narrow slowly-rotating radial streams, with $\beta \sim 1$, which ‘diffuse’ through the field.

12. The steady state that we find in Model B does not appear to have been identified in

any earlier simulations in the literature. Some of those simulations were not run long enough to achieve steady state, while others employed an incorrect ‘absorbing cylinder’ boundary condition which prevents the magnetic flux from accumulating near the black hole.

We thank Eliot Quataert for comments on the manuscript and helpful suggestions. IVI was supported by the U.S. Department of Energy (DOE) Office of Inertial Confinement Fusion under Cooperative Agreement No. DE-FC03-92SF19460, the University of Rochester, the New York State Energy Research and Development Authority, and RFBR grant 00-02-16135. RN was supported by NSF grant AST-9820686.

REFERENCES

- Abramowicz, M. A., Czerny, B., Lasota, J.-P., & Szuszkiewicz, E. 1988, *ApJ*, 332, 646
- Abramowicz, M. A., Björnsson, G., & Igumenshchev, I. V. 2000, *PASJ*, 52, 295
- Abramowicz, M. A., Chen, X.-M., Kato, S., Lasota, J.-P., & Regev, O. 1995, *ApJ*, 438, L37
- Abramowicz, M. A., Igumenshchev, I. V., & Lasota, J.-P. 1998, *MNRAS*, 293, 443
- Abramowicz, M. A., Lasota, J.-P., & Igumenshchev I. V. 2000, *MNRAS*, 314, 775
- Armitage, P. J., Reynolds, C. S., & Chiang, J. 2001, *ApJ*, 548, 868
- Balbus, S. A., & Hawley, J. F. 1991, *ApJ*, 376, 214
- Balbus, S. A., & Hawley, J. F., 2002, *ApJ*, 573, 749
- Bardeen, J. M. 1970, *ApJ*, 162, 71
- Begelman, M. C., & Meier, D. L. 1982, *ApJ*, 253, 873
- Blandford, R. D., & Payne, D. G. 1982, *MNRAS*, 199, 883
- Blandford, R. D., & Begelman, M. C. 1999, *MNRAS*, 303, L1
- Casse, F., & Keppens, R. 2002, *ApJ*, 581, 988
- Celotti, A., & Rees, M. J. 1999, *MNRAS*, 305, L41
- Chen, X., Abramowicz, M., & Lasota, J.-P., 1997, *ApJ*, 476, 61
- Christodoulou, D. M., Contopoulos, J., & Kazanas, D. 2002, preprint (astro-ph/0211511)
- Colella, P., & Woodward, P. R. 1984, *J. Comput. Phys.*, 54, 174
- Gilham, S. 1981, *MNRAS*, 195, 755
- Hawley, J. F. & Balbus, S. A., 2002, *ApJ*, 573, 738
- Hawley, J. F. 2000, *ApJ*, 528, 462
- Hawley, J. F. 2001, *ApJ*, 554, 534
- Hawley, J. F., Balbus, S. A., & Stone, J. M. 2001, *ApJ*, 554, L49
- Hawley, J. F., & Krolik, J. H. 2001, *ApJ*, 548, 348

- Hawley, J. F., & Krolik, J. H. 2002, ApJ, 566, 164
- Ichimaru, S. 1977, ApJ, 214, 840
- Igumenshchev, I. V., & Abramowicz, M. A. 1999, MNRAS, 303, 309
- Igumenshchev, I. V., & Abramowicz, M. A. 2000, ApJS, 130, 463
- Igumenshchev, I. V., Chen, X., & Abramowicz, M. A. 1996, MNRAS, 278, 236
- Igumenshchev, I. V., Abramowicz, M. A., & Narayan, R. 2000, ApJ, 537, L27
- Igumenshchev, I. V., & Narayan, R. 2002, ApJ, 566, 137
- Igumenshchev, I. V. 2002, ApJ, 577, 31
- Jaroszyński, M., Abramowicz, M. A., & Paczyński, B. 1980, Acta Astr., 30, 1
- Krolik, J. H. 1998, ApJ, 498, L13
- Krolik, J. H., & Hawley, J. F. 2002, ApJ, 573, 754
- Lasota, J.-P. 1996, in *Physics of Accretion Disks : Advection, Radiation and Magnetic Fields*, eds S. Kato, S. Inagaki, S. Mineshige, J. Fukue (Amsterdam: OPA), 85
- Machida, M., Matsumoto, R., & Mineshige, S. 2001, PASJ, 53, L1
- McKinney, J. C., & Gammie, C. F. 2002, ApJ, 573, 728
- Narayan, R., Igumenshchev, I. V., & Abramowicz, M. A. 2000, ApJ, 539, 798
- Narayan, R., Kato, S., & Honma, F. 1997, ApJ, 476, 49
- Narayan, R., Mahadevan, R., & Quataert, E. 1998, in *Theory of Black Hole Accretion Discs*, ed. M. A. Abramowicz, G. Björnsson, & J. E. Pringle (Cambridge: Cambridge Univ. Press), p148
- Narayan, R., & Yi, I. 1994, ApJ, 428, L13
- Narayan, R., & Yi, I. 1995a, ApJ, 444, 231
- Narayan, R., & Yi, I. 1995b, ApJ, 452, 710
- Narayan, R., Quataert, E., Igumenshchev, I. V., & Abramowicz, M. A. 2002, ApJ, 577, 295
- Paczyński, B., & Wiita, P. J. 1980, A&A, 88, 23

- Paczynski, B., & Abramowicz, M. A. 1982, ApJ, 253, 897
- Quataert, E., & Gruzinov, A. 2000, ApJ, 539, 809
- Rees, M. J., Phinney, E. S., Begelman, M. C., & Blandford, R. D. 1982, Nat, 295, 17
- Shvartsman, V. F. 1971, Soviet Astron., 15, 377
- Stone, J. M., & Norman, M. L. 1992, ApJS, 80, 791
- Stone, J. M., Pringle, J. E., & Begelman, M. C. 1999, MNRAS, 310, 1002
- Stone, J. & Pringle, J. E., 2001, MNRAS, 322, 461
- Tassoul, J.-L., 1978, *Theory of Rotating Stars* (Princeton: Princeton University Press)

Fig. 1.— Snapshot of the density distribution in Model A in the $x - z$ plane (meridional cross-section). The box shown has a size of $128 \times 128 R_g$, with the black hole at the center. Magnetized gas with a toroidal field is injected continuously within a torus at radius $\simeq 510 R_g$ (well outside the box shown here). The color bar on the side indicates the scale for $\log \rho$. Note that the gas is concentrated toward the equatorial plane (the horizontal axis) and increases toward the black hole. The fluctuations in the density are caused by convective motions. The two vertical polar funnels are filled with low-density matter.

Fig. 2.— Snapshot of the pressure distribution in Model A in meridional cross-section (see Fig. 1 for details). The color bar gives the scale for $\log P$. In the two vertical polar funnels, the pressure is very small as there is very little matter there.

Fig. 3.— Schematic evolution of a perturbed magnetic line in a differentially-rotating accretion flow. The unperturbed velocity is assumed to correspond to a Keplerian rotation profile. (a), (b), (c), (d) show the geometry of a magnetic line as a function of time. (a) shows a small initial perturbation of the line; (b), (c) the perturbed segment of the line is stretched by the Keplerian shear, and a magnetic loop is formed; (d) the field line reconnects and the magnetic loop separates from the line, causing a net amplification of the field strength relative to (a).

Fig. 4.— Snapshot of magnetic lines in Model A in the $x - y$ plane (equatorial cross-section). The box shown has a size of $64 \times 64 R_g$, with the black hole at the center. The component of field lines parallel to the plane is shown. Note the large number of magnetic loops, stretched in the azimuthal direction by the Keplerian rotation. The origin of the loops is schematically explained in Fig. 3.

Fig. 5.— Snapshot of magnetic lines in Model A in meridional cross-section for a box of size $64 \times 64 R_g$. The component of field lines parallel to the plane is shown. Except for the polar regions, the magnetic field elsewhere has a highly tangled morphology. This is the result of convection.

Fig. 6.— Snapshot of the distribution of the plasma $\beta \equiv P_g/P_m$ in Model A in meridional cross-section for a box of size $128 \times 128 R_g$. The color bar gives the scale for $\log \beta$. A complicated pattern is seen in the distribution of β . Regions of large β , or weak magnetic field, correspond to regions of reconnection and dissipation of magnetic energy. In the polar regions, where magnetic field has a more regular structure (see Fig. 5), the distribution of β is more homogeneous.

Fig. 7.— Snapshot of the distribution of specific entropy s in Model A in the meridional plane for a box of size $128 \times 128 R_g$. The color bar gives the scale for $\log s$. Note the complicated filamentary structure in the equatorial region and in the intermediate region between the poles and the equator. This is the result of field dissipation and convection. The two vertical polar funnels are filled with high-entropy low-density matter.

Fig. 8.— Time-averaged distribution of specific entropy s (left) and specific angular momentum ℓ (right) in Model A in meridional cross-section. The averaging has been done over about three Keplerian rotation periods measured at $R_{out} = 256 R_g$. One can see, comparing the left and right plots, that lines of constant s are closely aligned with those of ℓ in the wide equatorial region. This indicates that the convective accretion disk is marginally stable with respect to the Høiland criterion. Note that some features in distributions of s and ℓ in the equatorial region are due to circulation pattern shown in Fig. 10.

Fig. 9.— Snapshot of velocity streamlines in Model A in meridional cross-section, for a box of size $64 \times 64 R_g$. The component of streamlines parallel to the plane is shown. Except for the polar regions, the flow pattern consists of numerous vortices and eddies, the result of convective turbulence.

Fig. 10.— Same as in Fig. 9, but for the time-averaged flow. The averaging has been done over about three Keplerian rotation periods measured at $R_{out} = 256 R_g$. Instead of the large number of eddies seen in Fig. 9, one now sees large-scale meridional circulation patterns which are quite symmetric with respect to the equatorial plane. In the polar regions and in the vicinity of the black hole the streamlines are directed inward. In the innermost region, inside $10 R_g$, outflows are observed, but only near the equatorial plane.

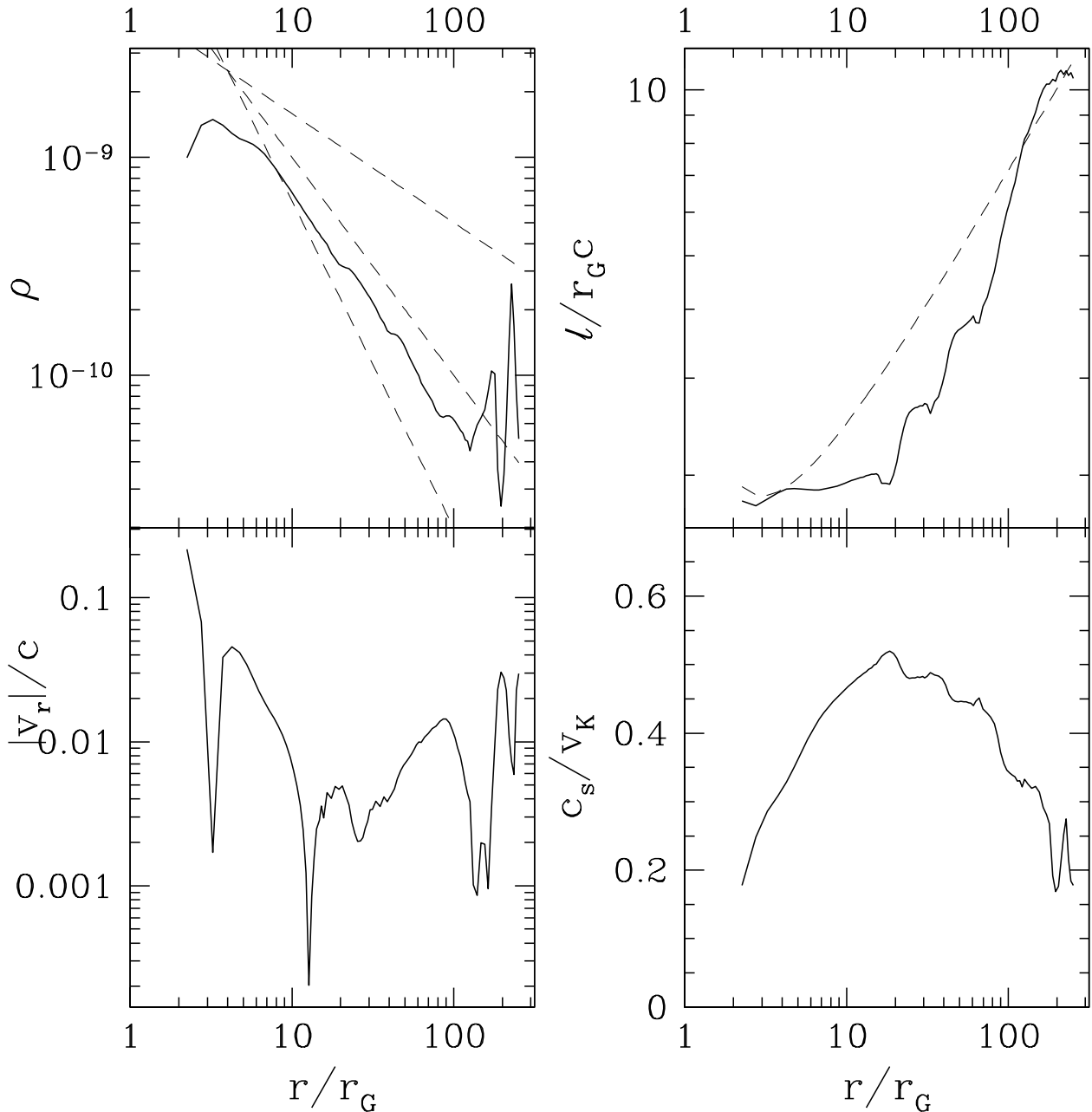


Fig. 11.— Radial structure of the flow in Model A on the equatorial plane. All plotted quantities – density ρ , specific angular momentum ℓ , radial velocity v_r , and sound speed velocity c_s – have been averaged over about three Keplerian periods measured at $R_{out} = 256R_g$. The density distribution is shown together with three dashed lines, which represent power-laws $\propto R^{-a}$ with $a = 1/2, 1, 3/2$. The specific angular momentum is shown along with a dashed line which represents the Keplerian distribution of ℓ for the pseudo-Newtonian potential (eq. 6) used in the simulation.

Fig. 12.— Time-averaged distribution of the $R\phi$ -component of the stress tensor, $T_{R\phi}$ (eq. [9]), in Model A in meridional cross-section for a box of size $128 \times 128 R_g$. The color bar gives the scale for the stress in units of the local time-averaged gas pressure. The black line separates regions of positive and negative stress (positive/negative stress correspond to outward/inward angular momentum flux, respectively). Note the correlation between the locations of negative and positive stresses and the time-averaged circulation pattern in Fig. 10 (remembering the different spatial scales in the two figures).

Fig. 13.— Density distribution in Model B in the $x-y$ plane (equatorial cross-section) at late times (steady state). The black hole is located at the center of a box of size $64 \times 64 R_g$. At this stage of the simulation, accretion occurs along almost radially directed streams moving in toward the black hole. One can see four symmetric streams in the image, which is the result of the simulation being done over a quarter of the domain, with azimuthally periodic boundary conditions (see §3).

Fig. 14.— Magnetic lines in Model B in the $x-z$ plane (meridional cross-section). The black hole is located at the center of a box of size $64 \times 64 R_g$. The component of field lines parallel to the plane is shown. The magnetic field clearly has a bipolar structure. The magnetic field is in rough equipartition with the accretion streams shown in Fig. 13.

Fig. 15.— Magnetic lines in Model B in equatorial cross-section for a box of size $64 \times 64 R_g$. Note the complicated structure of the field, which is loosely correlated with the positions of the accretion streams seen in Fig. 13.

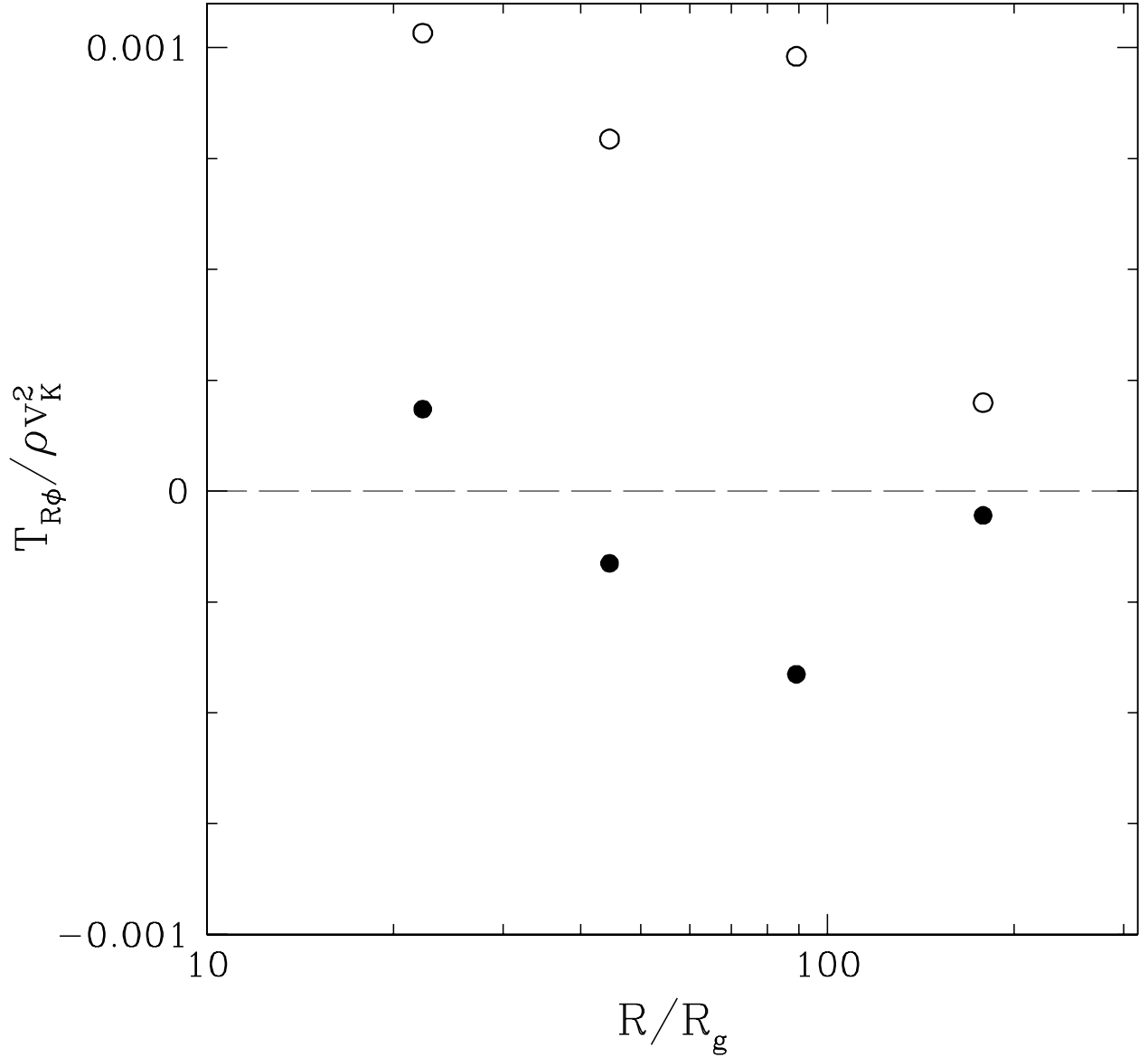


Fig. 16.— Radial distribution of Reynolds stress $T_{R\phi}^R$ (filled dots) and Maxwell stress $T_{R\phi}^{mag}$ (open circles) in Model A. The stresses have been averaged over spherical shells as described in the text. Note the negative sign of the Reynolds stress over a range of radius. In this region, convection transports angular momentum inward, in agreement with the fundamental postulate of the CDAF model. The positive sign of the Maxwell stress indicates that the magnetic field transports angular momentum outward. The total stress (sum of Reynolds and Maxwell stresses) is positive, as expected, so that on average the angular momentum is transported outward.

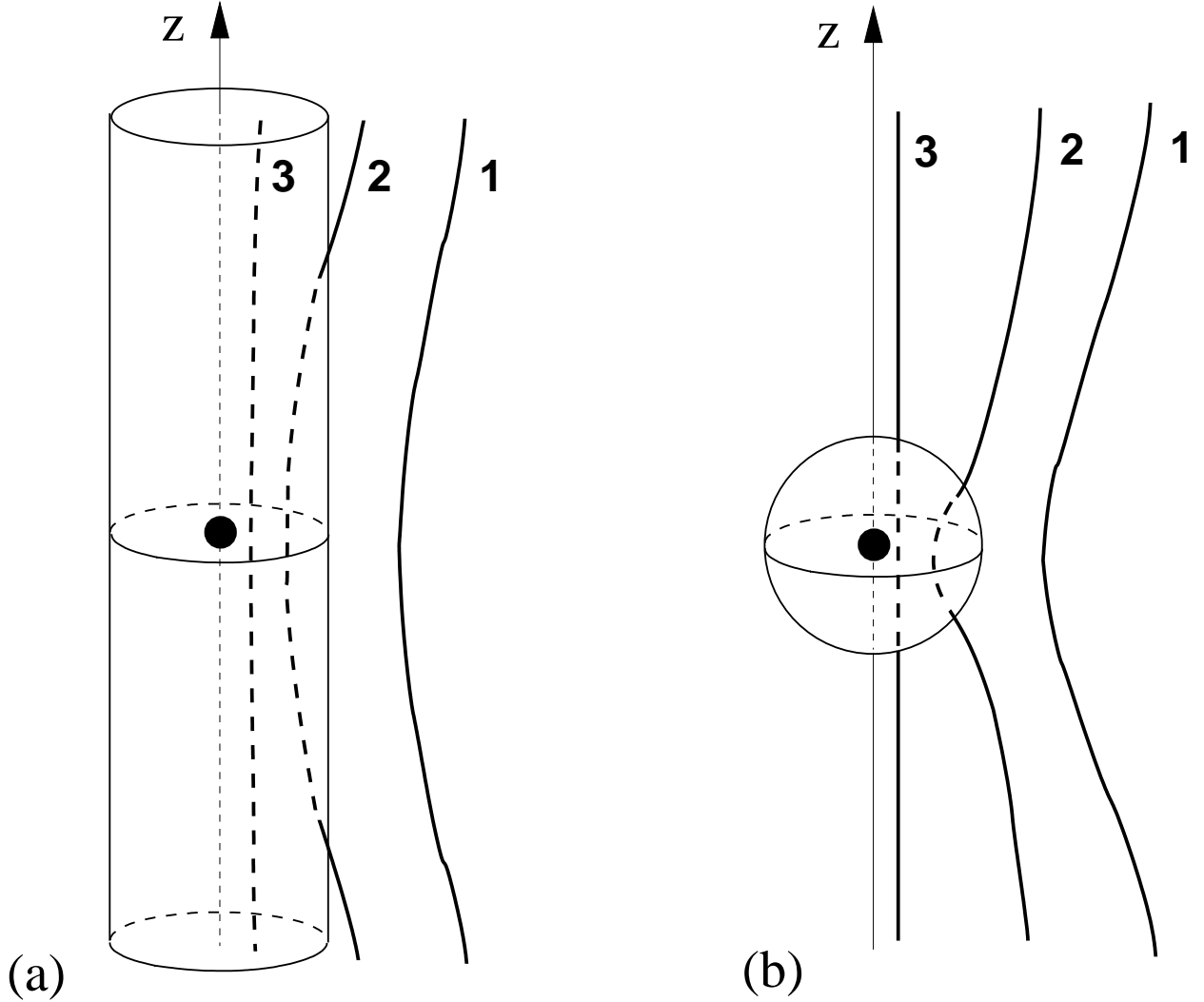


Fig. 17.— Cartoon depiction of the difference between two inner boundary conditions. Panel (a): shows the *absorbing cylinder* boundary condition used by Hawley et al. (2001) and Hawley & Balbus (2002). The cylinder goes through the whole computation domain, starting at the top outer boundary and ending at the bottom one. Panel (b): shows the *absorbing sphere* boundary condition used in the present study. The cylinder in panel (a) and the sphere in panel (b) indicate the locations of the absorbing boundaries in the two cases. Any matter or magnetic field that crosses the absorbing boundary stops contributing to the dynamics of the flow in the computational domain, thus mimicking the effect of gravitational capture of matter by the black hole. The bold lines 1, 2, 3 in each panel show the schematic time evolution of a frozen-in magnetic line as it is advected inward by the accretion flow. For simplicity, we do not consider here effects of rotation. In panel (a), the component of the magnetic field parallel to the z -axis is absorbed. Therefore, with time, a field line will disappear entirely from the computational domain (see line 3 which is entirely inside the absorbing cylinder). Thus, the simulation does not conserve the net magnetic flux. In panel (b), on the other hand, open field lines do not disappear when the accreting matter is absorbed by the black hole. Therefore, the net magnetic flux is conserved. This is shown by lines 2 and 3, which continue to contribute to the magnetic pressure around the black hole

This figure "f1.jpg" is available in "jpg" format from:

<http://arxiv.org/ps/astro-ph/0301402v1>

This figure "f2.jpg" is available in "jpg" format from:

<http://arxiv.org/ps/astro-ph/0301402v1>

This figure "f3.jpg" is available in "jpg" format from:

<http://arxiv.org/ps/astro-ph/0301402v1>

This figure "f4.jpg" is available in "jpg" format from:

<http://arxiv.org/ps/astro-ph/0301402v1>

This figure "f5.jpg" is available in "jpg" format from:

<http://arxiv.org/ps/astro-ph/0301402v1>

This figure "f6.jpg" is available in "jpg" format from:

<http://arxiv.org/ps/astro-ph/0301402v1>

This figure "f7.jpg" is available in "jpg" format from:

<http://arxiv.org/ps/astro-ph/0301402v1>

This figure "f8a.jpg" is available in "jpg" format from:

<http://arxiv.org/ps/astro-ph/0301402v1>

This figure "f8b.jpg" is available in "jpg" format from:

<http://arxiv.org/ps/astro-ph/0301402v1>

This figure "f9.jpg" is available in "jpg" format from:

<http://arxiv.org/ps/astro-ph/0301402v1>

This figure "f10.jpg" is available in "jpg" format from:

<http://arxiv.org/ps/astro-ph/0301402v1>

This figure "f12.jpg" is available in "jpg" format from:

<http://arxiv.org/ps/astro-ph/0301402v1>

This figure "f13.jpg" is available in "jpg" format from:

<http://arxiv.org/ps/astro-ph/0301402v1>

This figure "f14.jpg" is available in "jpg" format from:

<http://arxiv.org/ps/astro-ph/0301402v1>

This figure "f15.jpg" is available in "jpg" format from:

<http://arxiv.org/ps/astro-ph/0301402v1>